Hypersonic Ablation Modelling with Adaptive Mesh Refinement and Immersed Boundary Method

Monal Patel [1] *and Salvador Navarro-Martinez* [2]

Abstract

Adaptive mesh refinement and immersed boundary method are used to computationally study hypersonic ablation patterns. Ablation timescales are orders of magnitudes larger than flow time scales, making computational modelling of ablation problems only feasible if ablation is artificially sped-up. First, a subliming sphere at Mach 4 is investigated. It is found, that if the speed-up factor is small enough then the shape change due to ablation is independent of the speed-up factor. Then, a novel test case with a backward facing step with binary species ablating boundary under transitional flow conditions is created and investigated. Roughness is found to develop due to differential ablation and causes uneven surface recession, this promotes the generation of vorticity in the boundary layer. Cross-hatching ablation patterns are not observed in the current simulations, however, long-time simulations of the current case may lead to such patterns.

Keywords: *hypersonic, ablation, fluid-structure interaction, adaptive mesh refinement, immersed boundary method, moving boundaries*

Nomenclature

Latin
R – Universal gas constant
T – Temperature (K)
p – Pressure (Pa)
u – Velocity (m/s)
v – Wall normal velocity (m/s)
D – Diffusion coefficient (m^2/s)
q – Heat flux (W/m^{2}s)
h_{sg} – Enthalpy of sublimation (W/m^{2}s)
Y – Mass fraction
Re – Reynolds number

Da – Damkholer number
Greek
δ – length (m)
ρ – Density (kg/m^3)
τ – Timescale (s)
ω – Ablation flux (kg/m^{2}s)
Subscripts
k – Specie k
w – Wall
∞ – Free-stream

1. Introduction

Hypersonic ablation is a process in which a material surface erodes at high temperatures. It is driven by energy exchanges at the surface and results in surface mass loss. It is observed during controlled and uncontrolled atmospheric entry of satellites, spacecrafts and meteors. It is a complex fluid-structure interaction problem with multi-physics and multi-scale phenomena. There are various physical mechanisms which cause hypersonic ablation: phase changes (sublimation/evaporation and melting); surface (heterogeneous) chemical reactions; and spallation, which is the ejection of surface material due to thermal stresses. These result in the surface receding over time and often unevenly in space, generating surface patterns over a range of length scales, as shown in Fig. 1. Simple patterns like grooves and cross-hatching are thought to decay towards more complex patterns like regmaglypts (also known as scallops) found in meteorites.

---

[1]*Department of Mechanical Engineering, Imperial College London, monal.patel12@imperial.ac.uk*
[2]*Department of Mechanical Engineering, Imperial College London, s.navarro@imperial.ac.uk*
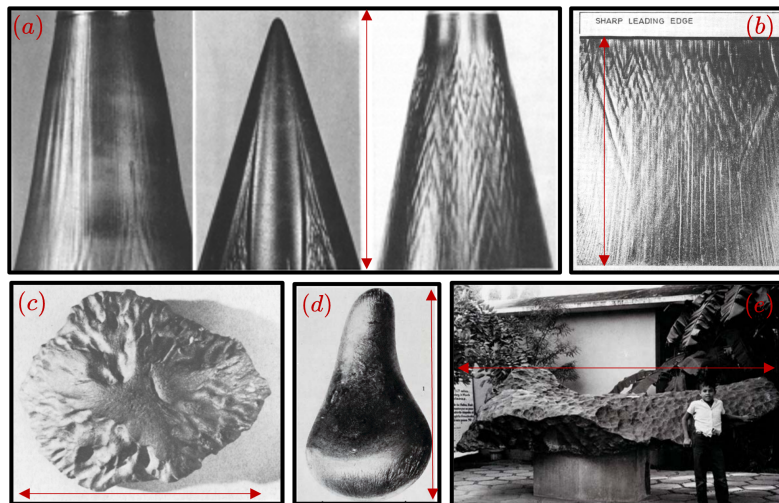
Fig 1. Hypersonic ablation surface patterns with indicated length scales. (a) From left to right, ablation grooves, turbulent wedge and cross-hatching patterns on wax cone (0.1m) [32]. (b) Flat plate cross-hatching pattern on wax ablator (0.15m) [33]. (c) The Middlesbrough stony meteorite, a smooth nose, few large and deep ablation pits followed by regmaglypt surface (0.16m) [18]. (d) A smooth pear-shaped iron meteorite (0.12m) [14]. (e) Bacubirito iron meteorite, world's longest meteorite, covered in regmaglypts (4.2m) [36].

There are several experimental and theoretical studies on hypersonic ablation that consider wall movement. They can be categorised as either larger scale shape change study or smaller scale surface patterns study.

Shape change studies. Simpkins [31] studied ablation shape change experimentally, beginning with an axis-symmetric Teflon body. They find that the body ablates towards an equilibrium profile. This profile is found to be independent of the initial nose profile obtained. Moreover, [21] study the effect of Reynolds number on shape change initially. They find that in low Reynolds number flows an initially hemispherical ablating body will evolve into a somewhat blunter shape. However, with higher Reynolds number conditions, an ogival-shaped nose forms due to increased heating as the flow transitions outside the nose. More recently, Bianchi and others [4] studied shape changes in low-temperature ablators, namely Camphor and Naphthalene, experimentally and computationally.

Pattern studies. Most experimental (lab and flight) and theoretical studies in the literature on hypersonic ablation patterns are from around the 1970s and focus on regular cross-hatching patterns. Most of these studies are reviewed and summarised by [34]. Regular cross-hatching patterns degrade towards regmaglypts. Regmaglypts are often found on meteors [18] and have not been characterised in the literature. They are expected to form in turbulent flow and the characteristic patterns length scale is likely linked to some flow length scale [5]. Only a handful of modern studies exist on hypersonic ablation patterns. They are mainly experimental and often complimented by computations of the experimental setup. [10, 39] study ablating surface recession in subsonic flow experiments and analytically. They study the problem analytically, without a computational fluid dynamic solver and by assuming simple boundary layer interaction with the surface. They stress that pattern formation is a balance between diffusive transfer from the surface to fluid and surface reaction mechanisms. They can calculate roughness length scale order of magnitude. Only computational study on hypersonic ablation patterns in the literature is by [37], completed independently and in parallel to the current study. They computationally study subliming low-temperature camphor ablator and observe localised grooves, but more complex patterns like cross-hatching and regmaglypt are not observed.

Difficulties in studying hypersonic ablation computationally are due to the problem's large range of space

and time scales. Surface recession rate due to ablation time scales are $O(1) - O(10)$s, whereas hypersonic simulation times are typically orders of magnitudes shorter, around $O(10^{-3})$ s. However, a computational approach has benefits over an experimental approach. It can de-couple physical mechanisms and may be able to give insights into mechanisms which are difficult to observe experimentally.

Adaptive mesh refinement (AMR) allows a range of length scales to be resolved efficiently, with automatic mesh generation even in complex flow-fields, when compared to body-fitted methods. Furthemore, AMR allows a local time-stepping, which is more efficient than a global time-stepping strategy in a multi-resolution flow-field.

Immersed boundary methods (IBM) [22] allow representation of complex geometries on structured grids. These methods require minimal changes to the flux derivative calculation unlike body-fitted approaches which require complex coordinate transformations. Furthermore, these methods are well suited to fluid-structure interactions when compared to body-fitted methods.

Recent numerical attempts to study ablation as a fluid-structure interaction problem with AMR-IBM [20, 1] focus on shape changes in laminar flow. In contrast, the current work focuses on hypersonic ablation pattern modelling in transitional flows where differential ablation occurs more easily.

1.1. Aims and outline
The aim of this paper is show a AMR-IBM approach to ablation modelling with moving boundaries and a first attempt at modelling an ablating surface with in transitional flow.

This paper is organised as follows. Sections 2 and 3 describe hypersonic ablation physical and numerical modelling. Section 3.2 tests the numerical method with a subliming sphere case. Lastly, Section 4 investigates a novel case with a transitional flow over a backward facing step case with an ablating surface.

2. Ablation modelling
Hypersonic ablation can be caused by four mechanisms: melting, sublimation/evaporation, heterogeneous reactions and spallation. The first two are most important and account for most of the mass loss [9]. Melting and evaporation-driven ablation involves a liquid phase and requires more complex modelling [3, 11, 26] compared to sublimation and spallation. Spallation is the ejection of solid particles from the ablating surface. It is generally the least important mode in hypersonic ablation; however, in some cases can be significant. For example, the Galileo probe could have had 10-30% of its ablation mass loss by spallation [6]. However, it remains poorly characterised with very few studies on the topic and remains a research area [13, 25]. Heterogenous reactions include Oxidation and Nitridation reactions and generally cause little mass loss compared with melting/evaporation or sublimation. Furthermore, they are only well characterised for carbon ablators. Hence, current work focuses on ablation by sublimation only.

Sublimation (and evaporation) are phase change reactions that are most simply described by Hertz-Knudsen (also known as Knudsen-Langmuir in sublimation-related literature) law. It is a balance of two terms, the first term represents the sublimation/evaporation flux of gaseous particles from the solid or liquid surface, and the second term represents the condensation flux of gaseous particles to the solid surface. The governing equation reads,

$$\omega_k = \alpha_k \sqrt{M_k/2\pi R T_w}(p_{e,k} - p_{w,k}). \tag{1}$$

Where α_k is an accommodation coefficient usually from experimental measurements or molecular dynamics simulations; M_k is the molar mass, T_w is the wall temperatures; $p_{w,k}$ is the species wall partial pressure. More detailed modelling of sublimation and evaporation is discussed by [7] and can include convective effects in a thin layer (also known as the Knudsen layer) around the surface. The equilibrium vapour pressure (p_e) can be estimated by a variety of semi-empirical fits [23]. The simplest [1] fit is also

---

[1]A more complex fit adds curvature to the log-linear Clausis-Claperyon relationship and is of the form $p_a = B\,exp(-C/(T_w + D))$. This is called the Antoine equation, where B, C, D are emperical constants.

known as the Clausius-Clapeyron relation:

$$p_{e,k} = p_{a,k}\exp(-h_{sg,k}/R_k T_w) = p_{a,k}\exp(-T_a/T_w) \tag{2}$$

Where $p_{a,k}$ is the activation pressure; $h_{sg,k}$ is the enthalpy of sublimation (or evaporation); $T_{a,k} = h_{sg,k}/R_k$ is an activation-like temperature.

Simply, sublimation governing law reads

$$\omega_k = A_k T_w^{-1/2}\left(e^{-T_{a,k}/T_w} - p_{w,k}/p_{a,k}\right), \qquad A_k = \alpha_k p_{a,k}\sqrt{M_k/2\pi R}, \tag{3}$$

where A_k is a constant. Therefore, sublimation (or evaporation) of a pure substance is a function of three parameters $(A_k, T_{a,k}, p_{a,k})$.

2.1. Surface balances

Multi-species ablation boundary conditions for subliming (non porous) and rigid ablators are simply steady state surface conservation balances [9], illustrated in Fig. 2.
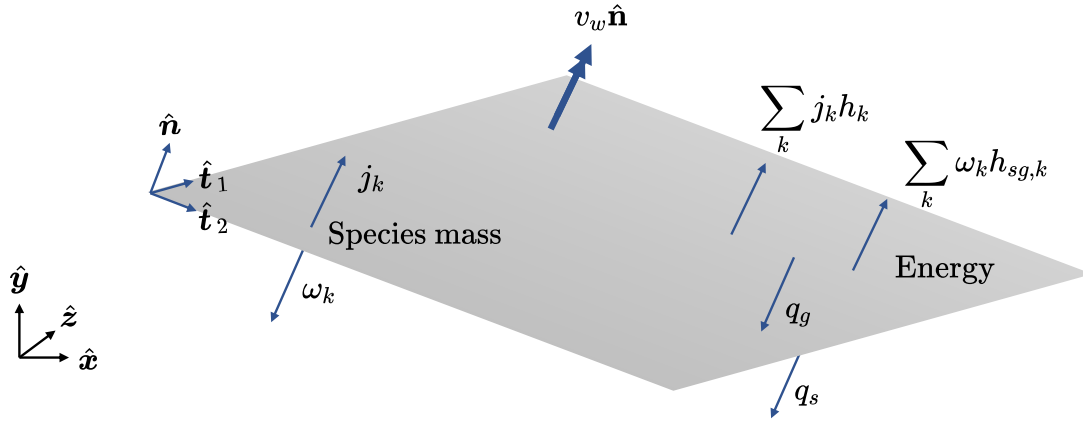

Fig 2. Surface species mass (left) and energy (right) balances $(\hat{x},\hat{y},\hat{z})$ and local $(\hat{n},\hat{t}_1,\hat{t}_2)$. Where v_w is the wall velocity due to ablation.

The species mass balance involves diffusive flux j_k balanced by species ablation rate ω_k. The momentum transfer is trivial as the wall is often rigid and restricted to moving in the wall-normal direction only (wall shear forces are irrelevant in the current study with ablation by sublimation only), and the dynamic pressure in the wall-normal direction is approximately zero as the wall moves very slowly. This means that the static pressure gradient is also approximately zero.

In the energy balance, the gas phase heat transfer to the surface (q_g) is balanced by the solid-phase heat transfer (q_s), heat transfer by mass transfer ($\sum_k j_k h_k$) and the enthalpy of phase change ($\omega_k h_{sg,k}$). Where $h_{sg,k}$ is the phase change enthalpy of species k.

The wall state is defined by the thermodynamic variables $\{\rho_w, \rho_{w,k}, v_w, T_w, p_w\}$ and geometric parameters $\{\hat{n}, \hat{t}_1, \hat{t}_2\}$. The number of conservation equations plus the equation of state equals the number of unknowns in the wall state vector. Mass, species mass, energy and wall-normal momentum surface conservation balances are therefore:

$$v_w = \sum_k \dot{\omega}_k/\rho_s; \quad j_k = \dot{\omega}_k''; \quad q_g = q_s + \sum_k \omega_k h_{sg,k} + \sum_k j_k h_k; \quad \left.\frac{dp}{dn}\right|_w = 0. \tag{4}$$

Where v_w is the wall recession velocity in the local coordinate system and can be transformed into a velocity vector in the global coordinate system.

For a binary system, the boundary conditions can be simplified by taking species 1 as the ablation species and species 2 as the free-stream species. Firstly, the diffusive wall species fluxes are:

$$\sum_k j_k = j_1 + j_2 = 0 \qquad \longrightarrow j_2 = -j_1 = -\omega_1 \tag{5}$$

So, the overall

$$v_w = \omega_1/\rho_s; \quad j_1 = \omega_1; \quad q_g = q_s + \omega_1(h_{sg,1} + h_1 - h_2); \quad \left.\frac{dp}{dn}\right|_w = 0. \tag{6}$$

3. Numerical method

This work uses an in-house continuum computational fluid dynamics solver, specially designed for modelling hypersonic flows with multi-species high-temperature thermochemical modelling and low numerical dissipation shock-stable flux calculation methods allow accurate modelling of turbulent flows. The solver operates in an structured (cartesian) adaptive mesh refinement (SAMR) framework [17]. The solver has been validated over a range of test cases, tested up to sub-orbital Mach numbers ($M \lesssim 30$). Another important feature of the solver is flow modelling around complex geometries with ghost point immersed boundary method (GPIBM) on a cartesian grid. Ghost point immersed boundary methods [38, 12] rely on approximating the closest point to the immersed boundary, called ghost point, in such a manner that it implies the correct boundary flux. Current work solves the following system of conservation laws :

$$\frac{\partial}{\partial t}\begin{pmatrix}\rho Y_1 \\ \rho Y_2 \\ \rho \\ \rho \boldsymbol{u} \\ \rho e_t\end{pmatrix} + \boldsymbol{\nabla} \cdot \begin{pmatrix}\rho Y_1 \boldsymbol{u} \\ \rho Y_2 \boldsymbol{u} \\ \rho \boldsymbol{u} \\ \rho \boldsymbol{u} \otimes \boldsymbol{u} + p\boldsymbol{I} \\ \rho \boldsymbol{u} h_t\end{pmatrix} + \boldsymbol{\nabla} \cdot \begin{pmatrix}\boldsymbol{j}_1 \\ \boldsymbol{j}_2 \\ 0 \\ -\boldsymbol{\tau} \\ \boldsymbol{q}_t - \boldsymbol{\tau} \cdot \boldsymbol{u}\end{pmatrix} = \boldsymbol{0}; \tag{7}$$

with the transport closures with Ficks law for mass diffusion and Fourier law for thermal conduction,

$$\boldsymbol{j}_1 = -\rho D_{12}\boldsymbol{\nabla}Y_1; \; \boldsymbol{j}_2 = -\rho D_{12}\boldsymbol{\nabla}Y_2; \; \boldsymbol{\tau} = \mu\left(\boldsymbol{\nabla}\boldsymbol{u} + (\boldsymbol{\nabla}\boldsymbol{u})^T - \frac{2}{3}\boldsymbol{\nabla}\cdot\boldsymbol{u}\boldsymbol{I}\right); \; \boldsymbol{q}_t = -\lambda\boldsymbol{\nabla}T + (\boldsymbol{j}_1 h_1 + \boldsymbol{j}_2 h_2). \tag{8}$$

Where ρ is density; $\boldsymbol{u}$ is the velocity vector; p is pressure; Y_1 and Y_2 are the species mass fraction; e_t is the total energy; $\boldsymbol{I}$ is the identity matrix; ∇ is the gradient operator; h_t is the total enthalpy; $\boldsymbol{j}_1$ and $\boldsymbol{j}_2$ are species mass diffusion flux vectors; τ is the shear stress tensor; and $\boldsymbol{q}_t$ is the thermal diffusion flux vector. The Euler fluxes are calculated via a 6th order accurate central-skew like conservative difference method with artificial dissipation based shock-capturing [8]. The viscous fluxes are calculated via 2nd order accurate standard central difference. The time integration uses explicit third-order TVD Runge-Kutta scheme [30], and with local time-stepping in the AMR framework.

Figure 3 illustrates the SAMR-GPIBM approach in two dimensions, where the grey curve represents the immersed boundary drawn on a hierarchical Cartesian grid. Immersed boundaries can be represented by a closed polygon (2D or 3D). In discrete space, it is represented by a set of elements (Σ_n) with vertices (Ω_n), where n is the body index. In 3D, the body is handled by a computational geometry library, GTS [24], for efficient element search and access operations. The library organises the geometry data in a tree structure allowing efficient access. The element size is similar to the local grid size. Set of points on i^{th} patch on level l is represented by P_i^l. On a given patch, each body separates a set of fluid points (Ω_f) and a set of body points (Ω_b). A body point directly adjacent to a fluid point is also part of a set of ghost points (Ω_g). The following relations hold between the sets of grid points:

$$\Omega_b \subseteq P_i^l; \quad \Omega_f \subseteq P_i^l; \quad \Omega_s \cap \Omega_f = \emptyset. \tag{9}$$

A ghost point's state is re-constructed using interpolation points (Ω_{ip}), image points (Ω_{im}) and immersed boundary points (Ω_{ib}).
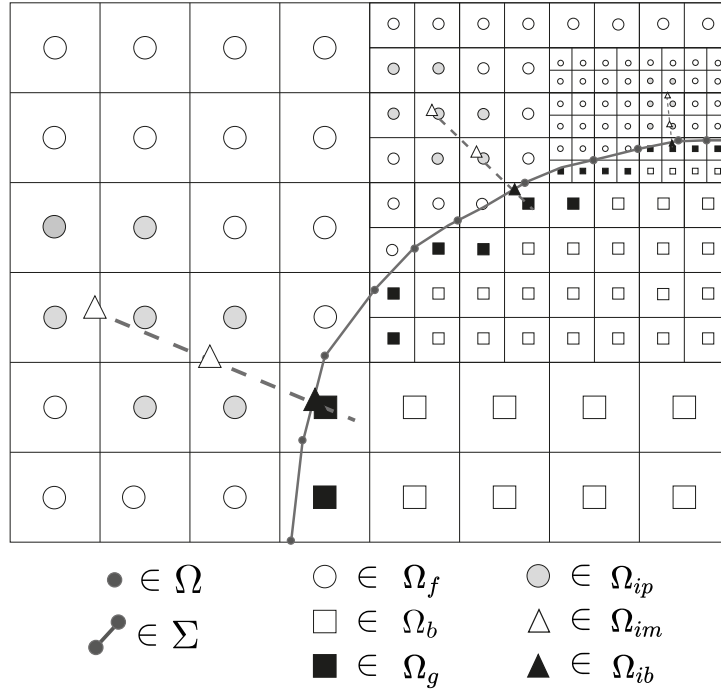
Fig 3. Structured adaptive mesh refinement with ghost point immersed boundary (SAMR-GPIBM).

3.1. Moving an ablating boundary

In this work, the solid (ablating) body surface is translated based on the local recession rate. The modifications to an immersed boundary solver to allow an ablating moving wall are described below:

1. *Immersed boundary point state (ϕ_{ib}) calculation.* The ablation BCs from Eq. (6) is used to calculate ϕ_{ib}. The boundary conditions need to be solved with an iterative Newton-Rhapson procedure as the state variables are non-separable in the energy equation, with the image-point state as the initial guess. For binary species, the boundary conditions can be written as:

$$\begin{pmatrix} f(Y,T) \\ g(Y,T) \end{pmatrix} = \begin{pmatrix} 0 \\ 0 \end{pmatrix} \tag{10}$$

   Where $f(Y,T)$ and $g(Y,T)$ are the mass and energy balance, respectively.

2. Translating the geometry vertices based on the elements recession velocity v_w.

3.2. Subliming sphere test

A simple single-species simulation is considered. No experiments with single species ablation in high-speed flow exist in the literature. The focus here is comparing with analytical stagnation point recession approximation and observing the effects of numerical speed-up on shape change. Secondly, a binary species is considered to validate the numerical method before simulations with surface patterns. The focus here is to observe shape change compared to camphor physical experiments. The fluid is nitrogen gas with a fictional ablating solid phase of nitrogen. Camphor experiments of [4] are used as a guide in the current setup to quantify the material properties of the fictional material. The non-dimensional numbers: the blowing factor (β) , material density ($\hat{\rho}_s$), activation temperature ($\hat{T}_a$) and activation pressure ($\hat{p}_a$) link the flow parameters with material as follows:

$$\beta = \frac{AT_r}{\rho_r u_r}; \qquad \hat{T}_a = \frac{T_a}{T_r}; \qquad \hat{\rho}_s = \frac{\rho_s}{\rho_\infty}; \qquad \hat{p}_a = \frac{p_a}{p_r}. \tag{11}$$

Where the subscript r represents the reference state. The non-dimensional variables, from Camphor experiment and current work are listed in Table 1. Where the reference thermodynamic quantities are

from stagnation state and reference velocity is the free stream velocity ($\rho_r = \rho_0; p_r = p_0; T_r = T_0; u_r = u_\infty$). The Mach and Reynolds numbers are decreased to increase the mesh size required to resolve the

Table 1. Non-dimensional ablation parameters.

	β	$\hat{T}_a$	$\hat{p}_a$	$\hat{\rho}_s$	Re_∞	M_∞
[4]	840	13	4	74	10^5	6
Current work	840	10	40	10^{-5}	10^4	4

flow and reduce computational cost. Ablating material density (ρ_s) controls the recession rate, as it is decreased by a factor of 10^{-7} to speed up ablation and allow a shorter simulation time. The dimensional parameters for the current case are:

$$A = 8.9 \times 10^4 \text{ kg s}^{-1}\text{m}^2\text{K}^{1/2}; \quad T_a = 6300 \text{ K}; \quad p_a = 2 \times 10^7 \text{ Pa}; \quad \rho_s = 2.6 \times 10^{-5} \text{ kg m}^{-3};$$

$$T_\infty = 150 \text{ K}; \quad u_\infty = 998 \text{ m s}^{-1}; \quad p_\infty = 4 \text{ Pa}.$$

The viscosity is modelled by Sutherland's law. Specific heat capacity is taken to be constant. Thermal conductivity satisfies constant Prandtl number($Pr = 0.7$). The global timestep is $5\mu s$ with CFL around 0.6. The flow time scale based on free-stream velocity is 1ms. Condensation is prevented during initialisation by enforcing $|\omega| > 0$.

3.2.1. *Without moving boundaries*

For a given body element size, a mesh refinement study is conducted. The sphere is constructed with 50K elements, arbitrarily chosen such that the average element size is (23 mm) [2] is visually small compared to the radius. The mesh with 3 levels of refinement is shown in Fig. 4. A single level of refinement is added near bow shock, in the shock layer in the front half of the sphere and around sphere walls. Further resolution is added to the front half of the sphere. Table 2 shows convergence of total ablation rate and stagnation point ablation rate with increasing mesh resolution.

Table 2. Single species subliming sphere mesh refinement.

Refinement levels	1	2	3	4
Number of points ($\times 10^6$)	3.4	6.0	12.9	39
Total Ablation rate ($\times 10^{-3}$kg s^{-1})	2.15	3.52	4.93	4.94
Stagnation point ablation rate ($\times 10^{-3}$kg s^{-1}m^{-2})	0.084	0.137	0.192	0.196

---

[2]Assuming equilateral triangle, its area is $A = l^2/2$. Where l is the element width.
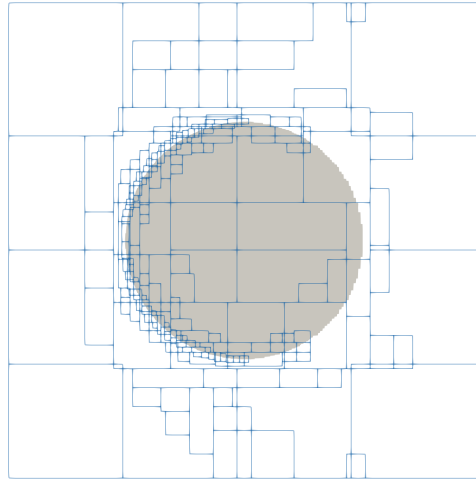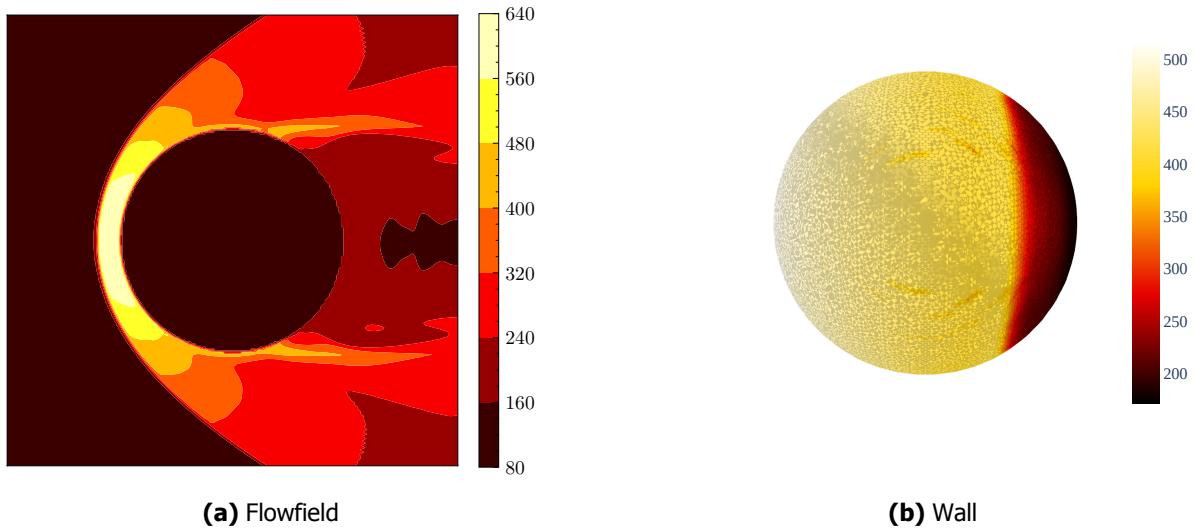
Fig 4. Slice of AMR patches around sphere with 3 refinement levels.

(a) Flowfield

(b) Wall

Fig 5. Single species subliming sphere temperature plots.

Analytically, as a first approximation, the stagnation point ablation rate can be estimated by:

$$q_0 = h_{sg}\omega \tag{12}$$

Where, q_0 is the stagnation point heat transfer calculated using semi-empirical correlations from [35]. The analytical approximate stagnation point wall temperature and ablation rate are, 492 K and 0.25 $\times 10^{-3}$kg s^{-1}m^{-2}. The simulation stagnation point wall temperature is 513 K, irrespective of the mesh resolution, around a 4% difference when compared to the analytical approximation. The flow stagnation point temperature is 630K, so the ablation cooling is evident. The sublimation rate is an exponential function of temperature, so, a small temperature change can result in large ablation cooling. This sensitivity is reduced by increasing β and reducing T_a/T_w. The ablation mass flux from simulations is around 60% larger than the analytical value.

3.2.2. *With moving boundaries*

Effect of ablation speed-up factor on shape change. A wall Damkholer number (Da_w) can be controlled to balance computational cost and accuracy:

$$Da_w = \frac{\tau_f}{\tau_w} = \frac{u_2}{v_w} = \frac{\rho_s u_2}{\omega_0}; \qquad \frac{u_2}{u_1} = \frac{M_\infty^2(\gamma - 1) + 2}{M_\infty^2(\gamma + 1)} \tag{13}$$

Da_w is defined as the ratio of the post-shock velocity to stagnation point wall recession velocity. In the current study, $Da_w = [5, 20, 40]$ are selected. These correlate to a very light solid with $\rho_s = [411, 1644, 3288] \times 10^{-6}$ kg/m^3.

Figure 6 shows the sphere shape slices varying with wall timescale (τ_w). A blunted-sphere shape forms over time. The shape change depends on the wall Damkholer number, until a critical value. After this, the shape change is independent of the wall Damkholer number. If Da_w is less than a critical value, then the ablation can be artificially sped-up without affecting the qualitative behaviour.

Figure 7 shows the shape change comparison with ablation due shear stress [19], hydrodynamic erosion on clay bodies. The results suggest that the sphere-cone shape, often found in meteors, cannot be formed by a sublimation ablation model only. For meteors, this conical shape is likely to occur due to melting and melt layer erosion by shear stress.
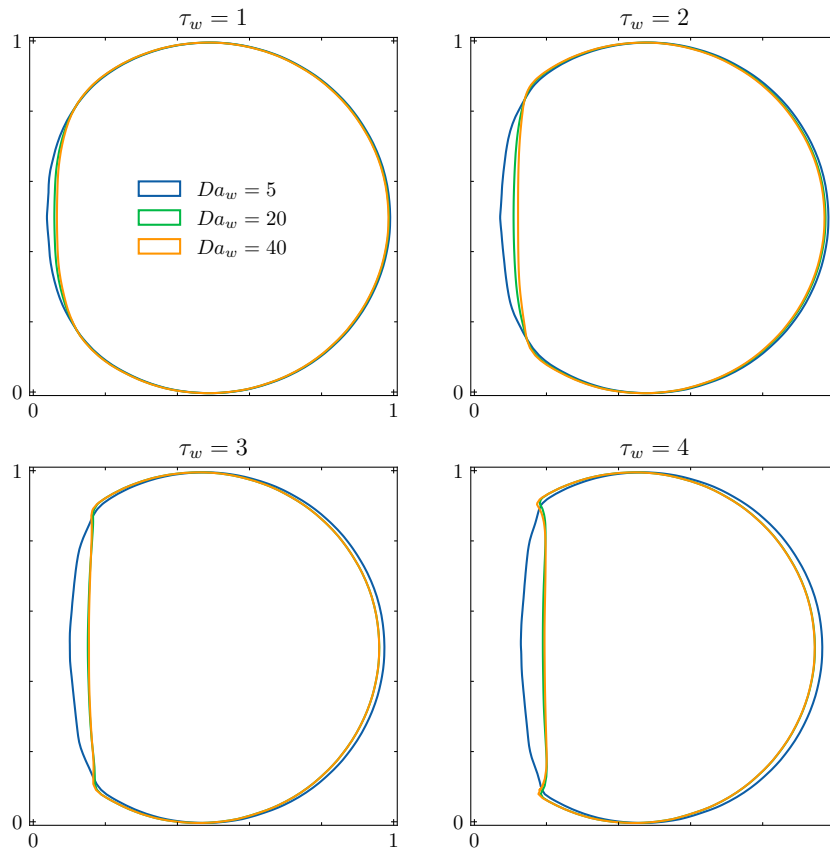

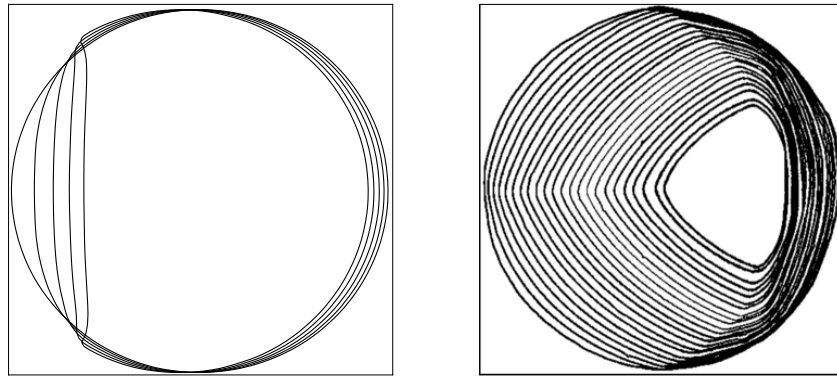**Fig 6.** Subliming sphere shape change with material time (τ_w).

Fig 7. Comparison of shape changes with different ablation modes. Left: Sublimation only (Current work). Right: Shear only [28].

4. Results

This section aims to re-produce the hypersonic ablation patterns numerically. Previously, [37] numerically studied cross-hatching patterns. They explored flows over cones and flat plates with roughness. They observed streamwise vortices but were not able to re-produce cross-hatching patterns.

The backward facing step (BFS) is selected as it can generate multiple streamwise vortices and trigger a quick transition to turbulence, without any external forcing [15]. Furthermore, lab experiments often lead to a BFS formation at the interface of the non-ablating and ablative material [33]. Channel BFS (internal flow) is much more widely studied [27, 2] than open BFS (external flow) [15, 16]. Supersonic external BFS is similar to Channel BFS, but no direct comparison studies exist. However, in both cases, post-step boundary layer re-attachment and concave streamlines induce streamwise Gortler-like vortices.

Numerical Setup. Figure 8 shows the BFS geometry, loosely based on [16, 2]. The solid is bigger than the computational domain by $\delta_0/2$ in all directions, where δ_0 is the displacement thickness of the inflow boundary layer, this is to avoid the solid boundary crossing the domain boundary during run time with moving boundaries. The inflow boundary layer is a polynomial fit of the exact solution of compressible boundary layer equations. The computational domain boundary conditions are periodic in y, zero-gradient in x and z. Table 3 summarises the flow conditions.
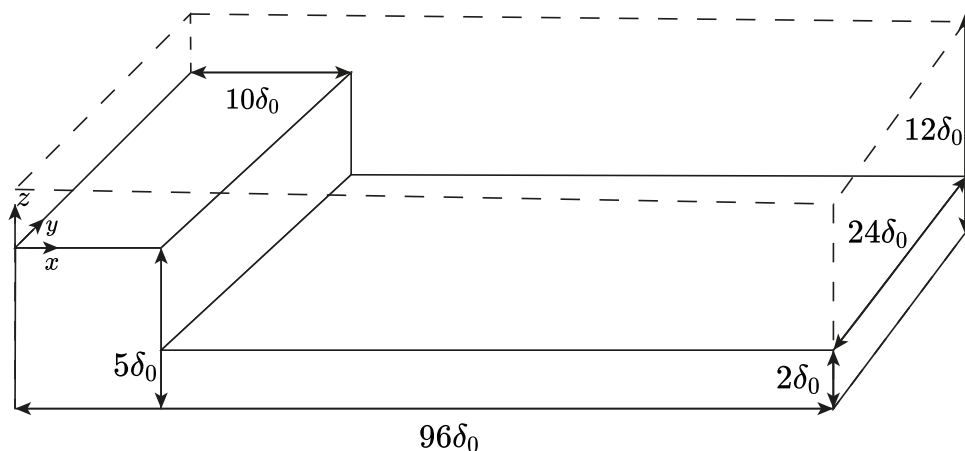

Fig 8. Backward facing step geometry and computational domain.

Where, δ_1 is the momentum thickness of the inflow boundary layer, δ_0 is the displacement thickness

Table 3. Backward facing step flow conditions.

M_∞	T_∞ (K)	P_∞ (Pa)	δ_1 (mm)	δ_0 (mm)	$Re_{\delta_0}/10^3$	δ_v (μm)	$x_0(m)$	τ_f (μs)
4	300	3000	0.82	1.56	4.02	17.3	0.15	106

of the inflow boundary layer, $Re_{\delta_0} = \rho_\infty u_\infty \delta_0/\mu_\infty$ and represents the Reynold's number based on displacement thickness, δ_v is the viscous length scale of the inflow boundary layer, x_0 is the inflow boundary layer distance from the start of a flat plate leading edge, and a flow time is defined as $\tau_f = 96\delta_0/u_\infty$.

The specific heat capacity at constant pressure (C_p) is taken as constant at 400K for camphor at 1040 kJ/kg and air as 1050 kJ/kg. The C_p for camphor varies by a factor of two within the 300-1000K range, much more than air. However, a constant C_p assumption is justified for the current study as fluid temperatures remain below 600K at all times and the variation in C_p will not affect the qualitative behaviour. Polynomial fits as functions of temperature for camphor transport properties [41], viscosity, thermal conductivity and binary diffusion coefficient are used. Whereas, Sutherland's law is utilised for air viscosity and thermal conductivity. Mixture properties are calculated using Wilke's mixing rule [40].

4.1. Mesh refinement

A mesh refinement study is conducted. The base mesh is $[512 \times 128 \times 64]$. Up to three refinement levels are added near walls and in the boundary layer. For all cases, the base mesh time-step (Δt) and steps per flow-time (N_τ) are 0.15 μs and 1000. The maximum CFL is around 0.7. Results from the three cases with increasing wall resolution are summarised in Table 4 and the finest case mesh is shown in Figure 9. The integrated heat load converges and the finest mesh is likely to be within 10% of the converged value. Hence, a high-resolution mesh is deemed sufficient for the remainder of the study. In all cases, the streamwise vortices generate spanwise variations in heat transfer, as expected. Figure 10shows the effect streamwise vorticies on surface heat transfer.

Table 4. Mesh

Resolution	Refinement levels	Points ($\times 10^6$)	$(\Delta y^+)_w$	Heat load (W)
Low	1	13	8	103
Medium	2	35	4	58
High	3	67	2	48
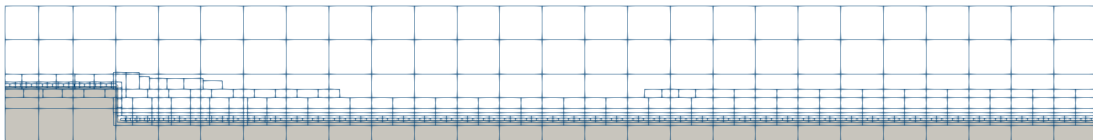
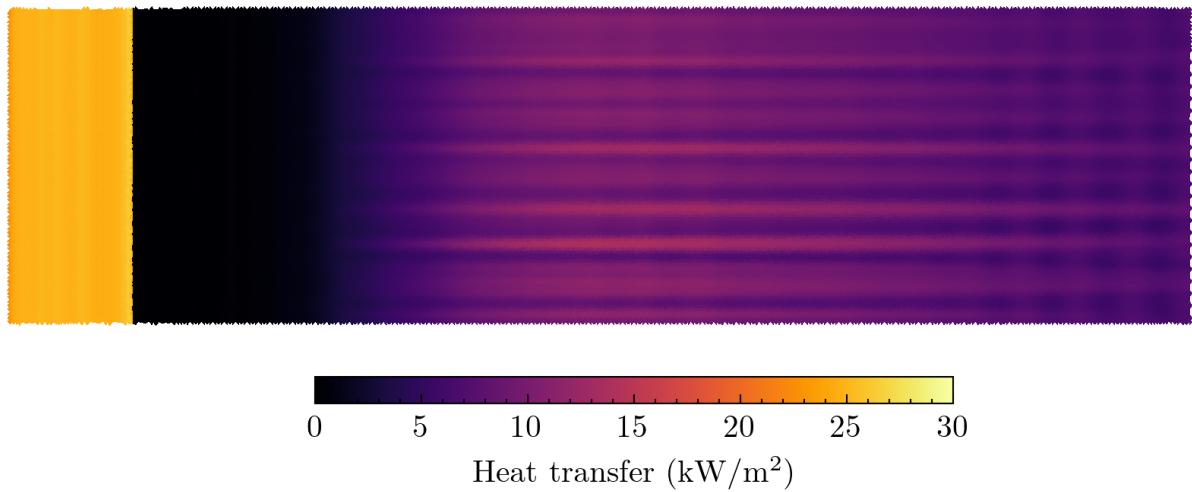**Fig 9.** Backward facing step AMR 3 level mesh with patch edges (blue lines).

**Fig 10.** Backward facing step wall steady-state heat transfer with high resolution mesh.

4.2. Moving wall ablation

The BFS case with a moving wall is investigated, where the local ablation rate controls the wall recession. The wall recession is performed by the numerical method described in Section 3.1. The initial computational domain state is from the fixed wall ablation steady state simulations.

Moreover, the equilibrium ablation wall temperature is approximately $361K$, calculated by assuming the inflow boundary layer heat transfer rate, free-stream pressure and assumed mass fraction of 0.5. This temperature is then used to calculate a reference ablation rate and set solid density, $\rho_s = 0.117$ kg/m^3 with $Da_w = 50$. The solid is moved every 10 steps and the maximum movement is limited to $\Delta x/2$, for numerical stability. The ablation boundary condition is only applied on the lower plate. The upper plate remains at a constant wall temperature of 300K. Figure 11 shows the instantaneous surface properties at $\tau_f = 1$ and $\tau_f = 2$. The following observations are made:

- Figure 11a suggests that the mass fraction in the re-circulation region is not zero because of the trapped ablated species within the region. The streamwise vortices induce a spanwise variation in the surface mass fraction, as observed at $\tau_f = 2$. This variation in mass fraction also contributes to the spanwise variation in ablation rate. An arrowhead pattern in ablation mass flux rate due to the streamwise vorticies forms. This differential ablation could lead to the formation of more complex patterns like cross-hatching patterns over a longer time. However, cross-hatching patterns do not form in the current simulations.

- Figure 11b suggests that the transitional flow over the backward facing step creates uneven surface ablation, and surface roughness develops. The surface ablates to a maximum depth of around $0.8\delta_0$, and the maximum surface height fluctuation is around $\pm 0.2\delta_0$. The surface recession increases with increasing distance downstream of the re-attachment line, and streamwise grooves seem to develop over time.

Figure 12 shows increased vorticity immediately after re-attachment point when compared to the initialisation with stationary wall ablation steady-state solution. This suggests that ablation-induced roughness maybe important for boundary layer stability and transition. The effect of distributed roughness on boundary layers remains an open problem, especially with roughness generated by ablation [29].
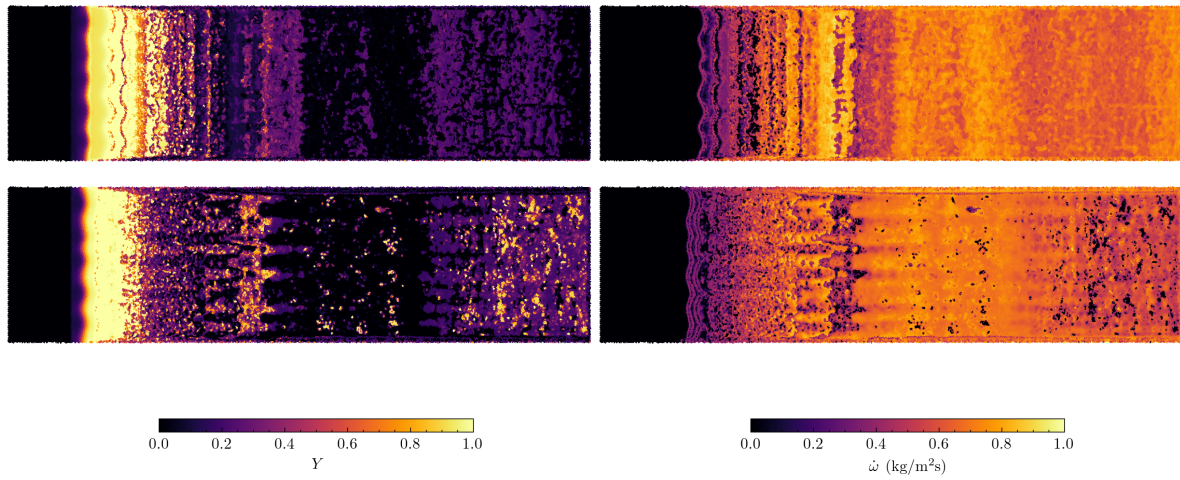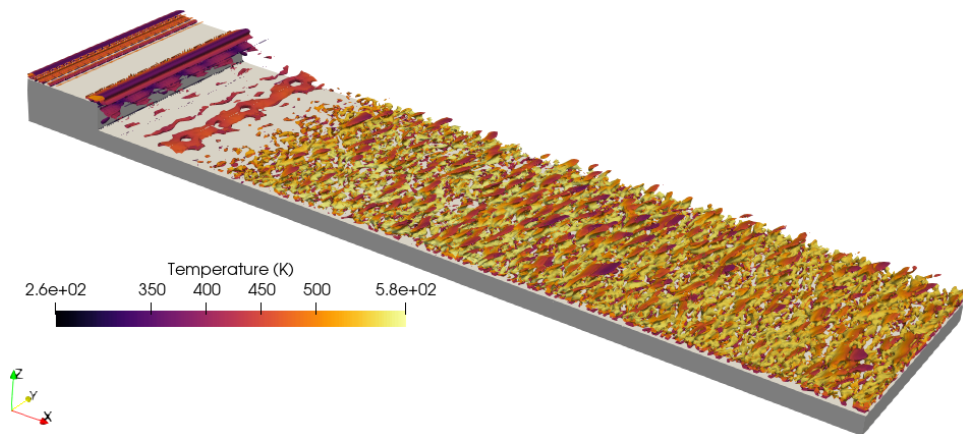
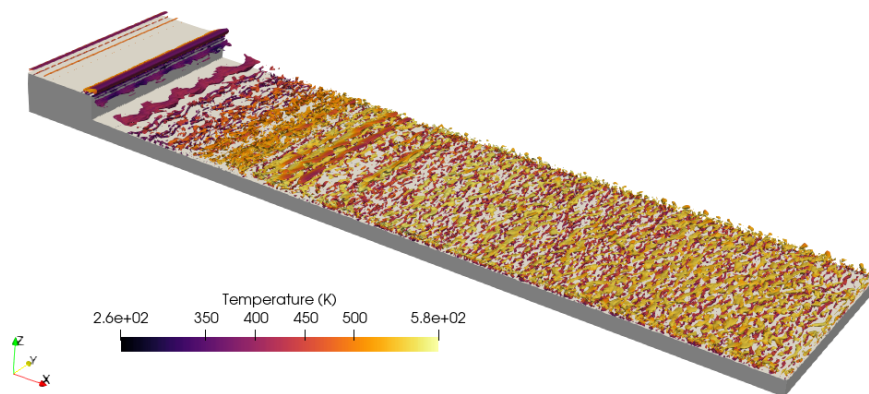**(a)** Ablating species mass fraction (left) and mass flux (right).
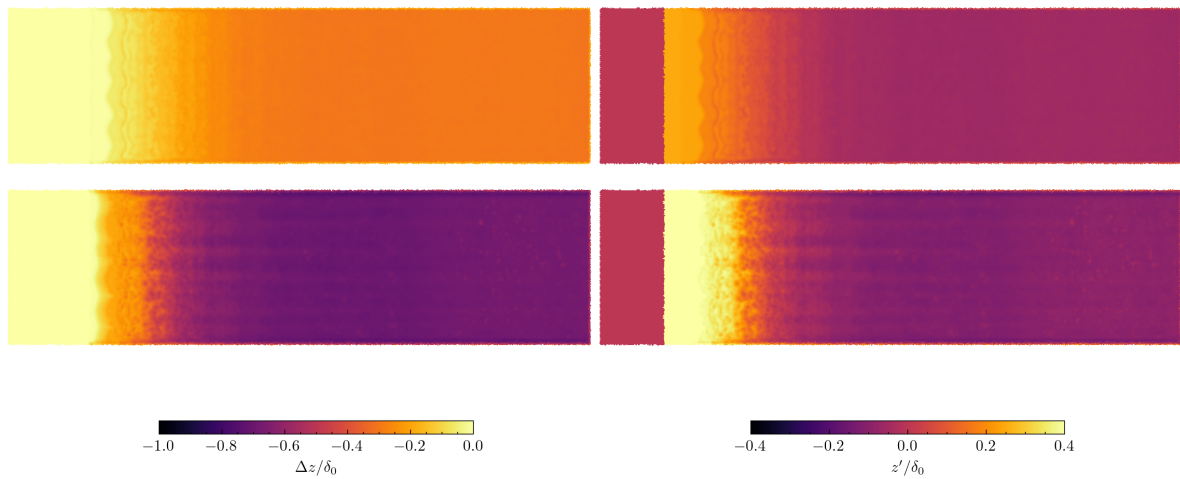
(b) Surface displacement (left) and surface height fluctuations (right) normalised by inflow boundary layer thickness (δ_0).
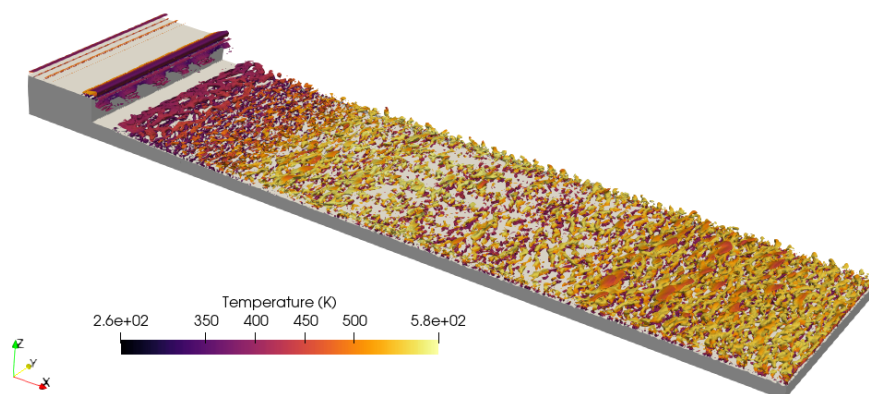
Fig 11. Surface properties with ablating and moving wall boundary condition at $\tau_f = 1$ (top row) and $\tau_f = 2$ (bottom row).

(a) $\tau_f = 0$

(b) $\tau_f = 1$

(c) $\tau_f = 2$

Fig 12. Q-criterion with temperature field colouring of iso-surfaces.

5. Conclusion

A study on hypersonic ablation with structure adaptive mesh refinement and ghost point immersed boundary method was conducted. The main challenge of the problem, from a computational perspective, is that the ablation timescales are orders of magnitudes larger than convective or simulation timescales.

Firstly, a simple validation test case was generated with single species ablation with a fictional solid state. The results show that, despite speeding up the ablation, if the speed-up factor is small then the shape change is independent of the speed-up factor. Another result is that ablation by sublimation is not sufficient to accurately model shape evolution of meteors.

Secondly, hypersonic ablation patterns are investigated. A novel backward facing step with binary species ablating boundary is created and investigated. A backward facing step is selected as it naturally generates streamwise vortices, which can cause localised heating. Also, hypothesised streamwise vortices are likely to be important in the generation of cross-hatching patterns. Three cases are simulated, without ablation, ablation with a stationary wall and ablation with a moving wall. These simulations suggest that ablation with a stationary wall destabilises the boundary layer and promotes the generation of vorticity. Moreover, roughness develops due to surface recession and it also seems to promote vorticity generation in the boundary layer. Hence, the ablation-generated surface roughness is likely to affect boundary layer stability and transition. Cross-hatching patterns are not observed in the current simulations, however, long-time simulations of the current case may lead to such patterns.

Future studies can explore the ablation topology of oriented Meteors. A motivation for this is to explore the possibility of predicting the meteor entry conditions with just the surface topology of the meteor and its material properties. This is important as meteor trajectories are rarely known. From a practical engineering perspective, a future study could focus on the effect of micro-meteoroid damage on ablative heat shields. Also, the effect of ablation generated roughness on boundary layer stability and transition could be investigated.

References

[1] Atkins, C., Charles, W., and Deiterding, R. (2022). A two-dimensional parallel strand/camr solver for hypersonic flow simulations. In *Proceedings of 33rd Parallel CFD International Conference*.

[2] Barkley, D., Gomes, M. G. M., and Henderson, R. D. (2002). Three-dimensional instability in flow over a backward-facing step. *Journal of fluid mechanics*, 473:167–190.

[3] Bethe, H. A. and Adams, M. C. (1959). A theory for the ablation of glassy materials. *Journal of the aerospace sciences*, 26(6):321–328.

[4] Bianchi, D., Migliorino, M. T., Rotondi, M., and Turchi, A. (2021). Numerical analysis and wind tunnel validation of low-temperature ablators undergoing shape change. *International Journal of Heat and Mass Transfer*, 177:121430.

[5] Bronshten, V. A. (2012). *Physics of meteoric phenomena*, volume 22. Springer Science & Business Media.

[6] Davuluri, R. S., Zhang, H., and Martin, A. (2016). Numerical study of spallation phenomenon in an arc-jet environment. *Journal of Thermophysics and Heat Transfer*, 30(1):32–41.

[7] Dias, B. (2020). *Thermal ablation and radiation modeling of meteor phenomena*. PhD thesis, UCL-Université Catholique de Louvain.

[8] Ducros, F., Laporte, F., Soulères, T., Guinot, V., Moinat, P., and Caruelle, B. (2000). High-order fluxes for conservative skew-symmetric-like schemes in structured meshes: application to compressible flows. *Journal of Computational Physics*, 161(1):114–139.

[9] Duffa, G. (2013). *Ablative thermal protection systems modeling*. American Institute of Aeronautics and Astronautics, Inc.

[10] Duffa, G., Vignoles, G. L., Goyhénèche, J.-M., and Aspa, Y. (2005). Ablation of carbon-based materials: investigation of roughness set-up from heterogeneous reactions. *International Journal of Heat and Mass Transfer*, 48(16):3387–3401.

[11] Feldman, S. (1959). On the instability theory of the melted surface of an ablating body when entering the atmosphere. *Journal of Fluid Mechanics*, 6(1):131–155.

[12] Ghias, R., Mittal, R., and Dong, H. (2007). A sharp interface immersed boundary method for compressible viscous flows. *Journal of Computational Physics*, 225(1):528–553.

[13] Grigat, F., Loehle, S., Zander, F., and Fasoulas, S. (2020). Detection of spallation phenomena on ablator surfaces. In *AIAA Scitech 2020 Forum*, page 1706.

[14] Hodge-Smith, T. (1939). Australian meteorites. *Australian Museum Memoir*, 7:1–84.

[15] Hu, W., Hickel, S., and Van Oudheusden, B. (2019). Dynamics of a supersonic transitional flow over a backward-facing step. *Physical Review Fluids*, 4(10):103904.

[16] Hu, W., Hickel, S., and Van Oudheusden, B. (2020). Influence of upstream disturbances on the primary and secondary instabilities in a supersonic separated flow over a backward-facing step. *Physics of Fluids*, 32(5):056102.

[17] Laboratory, L. B. N. (2014). Boxlib.

[18] Lin, T. and Qun, P. (1987). On the formation of regmaglypts on meteorites. *Fluid dynamics research*, 1(3-4):191–199.

[19] Mac Huang, J., Moore, M. N. J., and Ristroph, L. (2015). Shape dynamics and scaling laws for a body dissolving in fluid flow. *Journal of Fluid Mechanics*, 765.

[20] McQuaid, J. A., Zibitsker, A. L., Martin, A., and Brehm, C. (2022). Simulation of graphite ablation using an overset near body solver on an adaptive block-structured cartesian off-body grid. In *AIAA AVIATION 2022 Forum*, page 4088.

[21] Miller, I. M. and Sutton, K. (1966). An experimental study of the oxidation of graphite in high-temperature supersonic and hypersonic environments. Technical report, NASA.

[22] Mittal, R. and Iaccarino, G. (2005). Immersed boundary methods. *Annu. Rev. Fluid Mech.*, 37:239–261.

[23] Poling, B. E., Prausnitz, J. M., O'connell, J. P., et al. (2001). *The properties of gases and liquids*, volume 5. Mcgraw-hill New York.

[24] Popinet, S. (2006). The gnu triangulated surface library (gts).

[25] Price, K. J., Hardy, J. M., Borchetta, C. G., Panerai, F., Bailey, S. C., and Martin, A. (2020). Analysis of spallation products using arc-jet experiments. In *AIAA Scitech 2020 Forum*, page 1707.

[26] Raghunandan, P., Haskins, J. B., Palmer, G. E., Bessire, B. K., and Stern, E. C. (2021). Material response modeling of melt flow-vapor ablation for iron. *AIAA Journal*, pages 1–11.

[27] Rani, H., Sheu, T. W., and Tsai, E. S. (2007). Eddy structures in a transitional backward-facing step flow. *Journal of Fluid Mechanics*, 588:43–58.

[28] Ristroph, L., Moore, M. N., Childress, S., Shelley, M. J., and Zhang, J. (2012). Sculpting of an erodible body by flowing water. *Proceedings of the National Academy of Sciences*, 109(48):19606–19609.

[29] Schneider, S. P. (2008). Effects of roughness on hypersonic boundary-layer transition. *Journal of spacecraft and rockets*, 45(2):193–209.

[30] Shu, C.-W. and Osher, S. (1988). Efficient implementation of essentially non-oscillatory shock-capturing schemes. *Journal of computational physics*, 77(2):439–471.

[31] Simpkins, P. G. (1963). On the stable shape of subliming bodies in a high-enthalpy gas stream. *Journal of Fluid Mechanics*, 15(1):119–132.

[32] Stock, H. W. (1975). Surface patterns on subliming and liquefying ablation materials. *AIAA Journal*, 13(9):1217–1223.

[33] Stock, H. W. and Ginoux, J. J. (1973). Hypersonic low temperature ablation an experimental study of cross-hatched surface patterns. In *Astronautical Research 1971*, pages 105–120. Springer.

[34] Swigart, R. J. (1974). Cross-hatching studies-a critical review. *AIAA Journal*, 12(10):1301–1318.

[35] Tauber, M. E. (1989). A review of high-speed, convective, heat-transfer computation methods. *NASA Technical Report*.

[36] Terán-Bobadilla, E., Abundis-Patiño, J., Añorve, C., Moraila, C., Ortega-Gutiérrez, F., and Aragón-Calvo, M. (2017). On a novel geometric analysis of the bacubirito meteorite. *Earth, Moon, and Planets*, 120(2):101–111.

[37] Trevino, L. (2021). *Numerical Simulation of Surface Patterns on Sublimating Ablative Materials*. PhD thesis, University of Minnesota.

[38] Tseng, Y.-H. and Ferziger, J. H. (2003). A ghost-cell immersed boundary method for flow in complex geometry. *Journal of computational physics*, 192(2):593–623.

[39] Vignoles, G. L., Lachaud, J., Aspa, Y., and Goyhénèche, J.-M. (2009). Ablation of carbon-based materials: multiscale roughness modelling. *Composites Science and Technology*, 69(9):1470–1477.

[40] Wilke, C. (1950). A viscosity equation for gas mixtures. *The journal of chemical physics*, 18(4):517–519.

[41] Yaws, C. L. (2014). *Transport properties of chemicals and hydrocarbons*. William Andrew.